vinorelbine as induction chemotherapy followed by concomitant chemoradiotherapy for stage IIIB non-small-cell lung cancer: cancer and leukemia group B study 9431. *J Clin Oncol* 2002;**20**:4191–8.

20. Sekine I, Nokihara H, Sumi M *et al.* Docetaxel consolidation therapy following cisplatin, vinorelbine, and concurrent thoracic radiotherapy in patients with unresectable stage III non-small cell lung cancer. *J Thorac Oncol* 2006;**1**:810–5.

Radiation Protection Dosimetry Advance Access published December 16, 2014

Radiation Protection Dosimetry (2014), pp. 1–7 doi:10.1093/rpd/ncu357

WHOLE-BODY DOSE EVALUATION WITH AN ADAPTIVE TREATMENT PLANNING SYSTEM FOR BORON NEUTRON CAPTURE THERAPY

Kenta Takada[1,*], Hiroaki Kumada[2], Tomonori Isobe[2], Toshiyuki Terunuma[2], Satoshi Kamizawa[2], Hideyuki Sakurai[2], Takeji Sakae[2] and Akira Matsumura[2]
[1]Graduate School of Comprehensive Human Sciences, University of Tsukuba, 1-1-1, Tennodai, Tsukuba, Ibaraki 305-8575, Japan
[2]Faculty of Medicine, University of Tsukuba, 1-1-1, Tennodai, Tsukuba, Ibaraki 305-8575, Japan

*Corresponding author: takada@md.tsukuba.ac.jp

Received 16 September 2014; revised 14 November 2014; accepted 19 November 2014

Dose evaluation for out-of-field organs during radiotherapy has gained interest in recent years. A team led by University of Tsukuba is currently implementing a project for advancing boron neutron capture therapy (BNCT), along with a radiation treatment planning system (RTPS). In this study, the authors used the RTPS (the 'Tsukuba-Plan') to evaluate the dose to out-of-field organs during BNCT. Computed tomography images of a whole-body phantom were imported into the RTPS, and a voxel model was constructed for the Monte Carlo calculations, which used the Particle and Heavy Ion Transport Code System. The results indicate that the thoracoabdominal organ dose during BNCT for a brain tumour and maxillary sinus tumour was 50–360 and 120–1160 mGy-Eq, respectively. These calculations required ~29.6 h of computational time. This system can evaluate the out-of-field organ dose for BNCT irradiation during treatment planning with patient-specific irradiation conditions.

INTRODUCTION

Boron neutron capture therapy (BNCT) is a radiotherapy method that utilises the nuclear reaction between thermal neutrons and the ^{10}B isotope. The basic principle of BNCT was first proposed by Locher[1], and it has recently gained attention for its use in cell-selective radiotherapy. BNCT has previously been performed with neutrons obtained from nuclear reactors, although efforts are underway to generate these neutrons using particle accelerators[2]. A team led by the University of Tsukuba, and including the High Energy Accelerator Research Organization, the Japan Atomic Energy Agency, Hokkaido University, the Ibaraki Prefectural Government and Mitsubishi Heavy Industry Co., is currently engaged in a project to perform BNCT with an accelerator, and a treatment planning system is also being developed. Developing code is named the 'Tsukuba-Plan'[3].

When administering radiotherapy, pre-treatment dose calculations are performed using the patient's medical images. These dose calculations are known as radiation treatment planning (RTP). During RTP for BNCT, the dose calculation is performed by using the Monte Carlo algorithm, which incorporates the complex behaviour of neutrons with the need for accurate tracking of multiple radiation beams. The Monte Carlo algorithm is also used for other radiotherapies[4–6], although it is used less frequently in these therapies than that in BNCT.

To date, RTP for BNCT has focused exclusively on the dose to which in-field skin, tumour and nearby organs are subjected. As dose calculations are performed using the Monte Carlo algorithm, accurate calculations may require a long computational time. For broader areas, even more computational time is required to calculate the relevant dose. Furthermore, if a fine calculation mesh size is selected for calculations, the computational time extends even further.

Recently, numerous reports have described the effect of undesirable radiation doses on implanted medical devices and have evaluated the risk of developing secondary cancer due to the radiotherapy[7–10]. For these evaluations, the dose must be calculated for a broad area. Unfortunately, it is difficult to accurately calculate the undesirable radiation dose that is received over a wide area during BNCT.

In this study, the authors carried out whole-body dose evaluation during BNCT using the Tsukuba-Plan, which is currently under development. In addition, they verified the feasibility of simultaneously evaluating the undesirable dose for various organs during the RTP for BNCT.

MATERIALS AND METHODS

This research consists of two parts of sections. The calculation values for the thermal neutron fluence rate and the photon dose rate in a water phantom

© The Author 2014. Published by Oxford University Press. All rights reserved. For Permissions, please email: journals.permissions@oup.com

Downloaded from http://rpd.oxfordjournals.org/ at Tsukuba Central Library (Serials) on February 25, 2015

were compared with the measurement value under the same irradiation conditions (Section 1). Then, the authors evaluated the undesirable radiation dose for the out-of-field organs in BNCT using a whole-body phantom (Section 2).

The Tsukuba-Plan is capable of producing multiple-type input files that can be used for several Monte Carlo dose calculations. The Monte Carlo code used in this study was the Particle and Heavy Ion Transport code System (PHITS)[11]. The PHITS can transport and calculate various particles with wide energy ranges, such as neutrons, photons and other charged particles, allowing one to calculate all radiations relevant to BNCT. The PHITS is also highly flexible and suitable for use in a parallel computing environment. A parallel processing computer (70 cores, CPU: Xeon, 2.40 GHz) was used for calculations.

The authors assumed the epithermal neutron beam from Japan Research Reactor No. 4 (JRR-4) as the irradiation field for BNCT.

Confirmation of beam source in Tsukuba-Plan using a water phantom study

To confirm the JRR-4 beam could correctly output from the Tsukuba-Plan, the authors compared the actual measurement value from a water phantom with those calculated using the authors' system. The measurement values were obtained from a previously published study[12]. The thermal neutron fluence rate was measured by using the gold foil activation method[12, 13].

The thermal neutron fluence rate and photon dose rate at the central axis of the phantom were calculated using the Monte Carlo and the parallel processing computer. The water phantom had a diameter of 18.6 cm and a length of 24 cm. The walls were constructed of 3-mm-thick polymethylmethacrylate, and its interior was filled with water. The water phantom was placed 10 mm from the beam aperture, in the same position used during actual measurements.

Evaluation of the undesirable radiation dose for various organs during BNCT

BNCT for a brain tumour

The authors evaluated the undesirable radiation dose for various organs during BNCT irradiation of a brain tumour, using a whole-body phantom (PBU-10, Kyoto Kagaku Co., Ltd.). Computed tomography images of the phantom were acquired (5 mm of slice thickness, >250 images), and the tumour and various organs were defined. The clinical target volume (CTV) was defined as a virtual brain tumour in the left temporal lobe. The undesirable radiation doses for the thyroid gland, lungs, heart, spinal cord and liver were evaluated in the supine position.

The Tsukuba-Plan is capable of constructing voxel models in various sizes. In this study, the authors set the voxel size for the whole-body phantom at 8 pixels × 8 pixels × slice thickness (pixel space: 0.8 mm, slice thickness: 5 mm). The Monte Carlo calculation was performed until the statistical uncertainty of the neutron fluence rate in the liver was <5 %.

During BNCT treatment, the accumulated concentration of boron in the organs determines the total dose. The authors assumed a boron concentration of 24 ppm in normal tissue and set the concentration in the tumour region at three times that in the normal tissue. The boron concentration in the skin was set at 1.2 times the concentration in the normal tissue. Compound biological effectiveness (CBE) is a value that expresses the biological effectiveness due to the reaction between boron isotopes and neutrons and is dependent for each boron compound. In this study, the authors proposed RTP using boronophenylalanine, and the CBE for the tumour, normal tissue and skin was set at 3.8, 1.35 and 2.5, respectively.

In BNCT, relative biological effectiveness (RBE) values according to the kind of radiations are required. In this study, the RBE values for the thermal neutron (major interaction between neutrons and nitrogen) and the fast neutron (major interaction between neutrons and hydrogen) were set at 2.5[14]. The RBE value for the photons was set at 1.0[14].

The CBE values for the other organs were set at 2.3 for the lungs[15], 1.35 for the spinal cord[16] and 4.25 for the liver[15]. The CBE values and boron concentrations for the thyroid gland and heart were set at the same value as for normal tissue. The boron concentrations and weighting coefficients (CBE and RBE values) used in this study are summarised in Table 1. The irradiation time was set such that the normal brain received a weighted dose of <13 Gy[17].

Table 1. Boron concentrations and CBE values for the organs used in this study.

Tissue organ	Boron concentration (ppm)	CBE for BPA
Tumour	72 (T/N ratio: 3)	3.8
Normal tissue	24 (T/N ratio: 1)	1.35
Skin	28.8 (T/N ratio: 1.2)	2.5
Thyroid	24 (T/N ratio: 1)	1.35
Lung		2.3
Heart		1.35
Spinal cord		1.35
Liver		4.25

RBE values: 2.5 for the thermal neutron and fast neutron, 1.0 for photon (these values are same as internal organs). T/N ratio: the boron concentration ratio to normal tissue.

Downloaded from http://rpd.oxfordjournals.org/ at National Cancer Centre (JMLA) on February 5, 2015

BNCT for a maxillary sinus tumour

BNCT is also used to treat head and neck cancers[18–20] and may be performed with the patient in the seated position. The authors used the same phantom for the dose evaluation, and the CTV was defined as a virtual tumour in the left maxillary sinus. The undesirable radiation doses for various organs were evaluated in the seated position. In general, the tolerance dose for healthy organs, such as skin, is a factor that restricts irradiation time during BNCT. Thus, the authors also defined an area of skin (corresponding to the exposure site) as a region of interest. The Monte Carlo calculation was performed until the statistical uncertainty of the neutron fluence rate in the liver was <5 %. The irradiation time was set such that the skin within the irradiated field received a weighted dose of <15 Gy[19].

RESULTS

Water phantom study

The depth distribution of the thermal neutron fluence rate in the central axis of the phantom is shown in Figure 1. The vertical axis indicates the thermal neutron fluence rate, whereas the horizontal axis indicates the depth (in mm) from the surface of the phantom. The thermal neutron fluence rate from the Monte Carlo calculation was normalised using the maximum measurement value for the thermal neutron fluence rate. The values calculated using the authors' system were consistent with the measured values. The depth distribution of the photon dose rate on the central axis of the phantom is shown in Figure 2. The vertical axis indicates the photon dose rate. The measurement values for the photon dose rate were measured by using thermoluminescence dosemeter (TLD)[12, 21], and Kumada *et al.* have reported that the TLD used to obtain these measured values has an uncertainty of ~11 %[12], which was considered the uncertainty for the actual measured values (1 standard deviation).

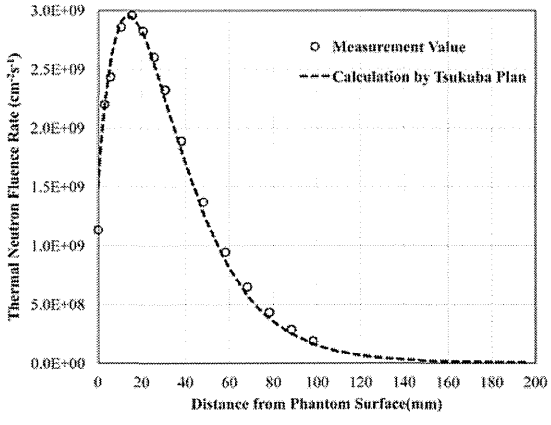

Figure 1. Comparison of the depth distribution for the thermal neutron fluence rate in the water phantom. The measurement values from (12) were used as the reference values.

Undesirable radiation dose for various organs during BNCT

BNCT for a brain tumour

The dose volume histogram (DVH) for various organs, including the CTV, is shown in Figure 3. The horizontal axis is the weighted dose (Gy-Eq), which was calculated as the sum of the various dose components, after each had been multiplied by the RBE values and the CBE for the boron compound[22]. Figure 4 shows an expanded DVH for the undesirable radiation doses to the out-of-field organs, and Table 2 shows the averaged dose ($D_{average}$) for various organs. These results indicate that the undesirable out-of-field radiation dose was 50–360 mGy-Eq during BNCT irradiation of a brain tumour in the supine position.

BNCT for a maxillary sinus tumour

Figure 5 shows an expanded DVH for the undesirable out-of-field radiation doses for various organs during BNCT irradiation of a maxillary sinus tumour, and Table 3 shows the $D_{average}$ for various organs. These results indicate that the undesirable out-of-field radiation dose during BNCT irradiation of a maxillary sinus tumour was highest in the thyroid gland (1.16 Gy-Eq) and was 120–360 mGy-Eq in the other organs.

DISCUSSION

Interest in the effect of radiotherapy on out-of-field organs has increased in recent years, and dose

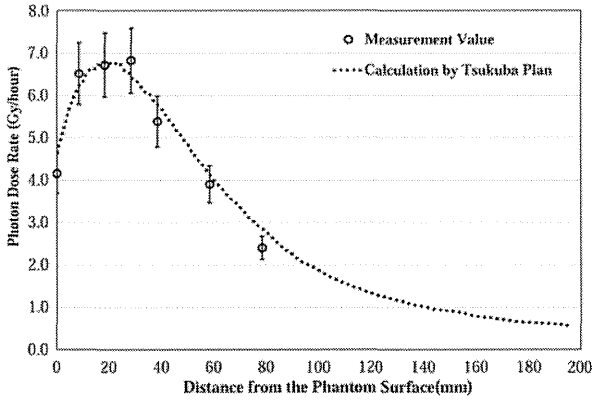

Figure 2. Comparison of the depth distribution for the photon dose rate in the water phantom. The measurement values from (12) were used as the reference values.

Downloaded from http://rpd.oxfordjournals.org/ at Tsukuba College of Technology on May 9, 2013

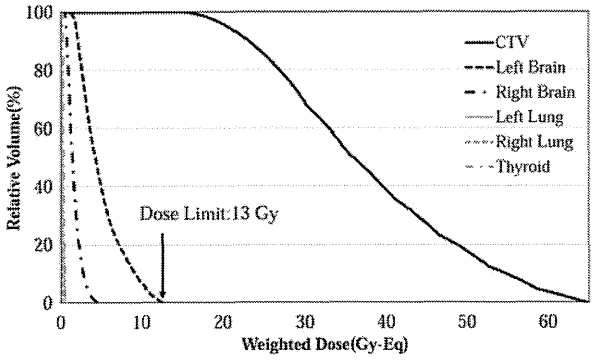

Figure 3. DVH for various organs, including the CTV, during BNCT for a brain tumour.

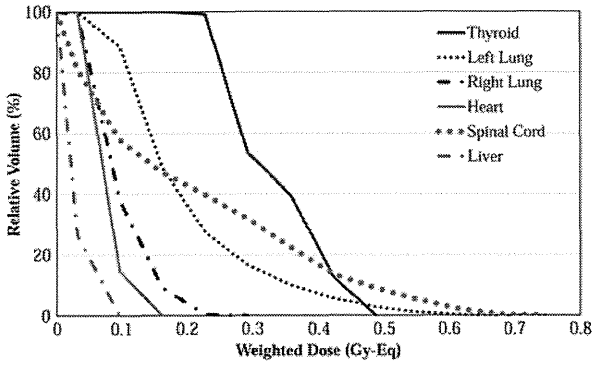

Figure 4. Expanded DVH of the undesirable dose for out-of-field organs during BNCT for a brain tumour in the supine position.

evaluation for out-of-field organs has been performed for BNCT[23, 24]. Tsukamoto *et al.* has reported the whole-body exposure with phantom experiment for cyclotron-based epithermal neutron beam[24]. They evaluated the undesirable dose for each organ by RBE-weighted dose in BNCT irradiation with the supine position. It is shown that the undesirable dose for the thyroid was larger compared with other organs in the report. Also, the larger contribution of the photon dose was also described. In order to provide the BNCT treatment safely, it is important to perform various evaluations about the undesirable dose with BNCT irradiation. In this study, the authors attempted to simultaneously evaluate the undesirable dose for out-of-field organs during RTP for BNCT with Tsukuba-Plan.

During BNCT, the biologically weighted dose is important. However, evaluating the weighted dose for organs throughout the body requires that the boron concentration that accumulates in each organ be set, along with the CBE for that organ. In addition, large numbers of medical images must be imported for this calculation. In this study, the authors were able to achieve both of these tasks, a significant achievement that enables patient-specific, whole-body, weighted

Table 2. $D_{average}$ at various organs, including the CTV, during BNCT for a brain tumour in the supine position.

Organ	$D_{average}$ (Gy-Eq)
CTV	37.5
Thyroid	0.36
Right lung	0.13
Left lung	0.23
Heart	0.11
Spinal cord	0.23
Liver	0.05

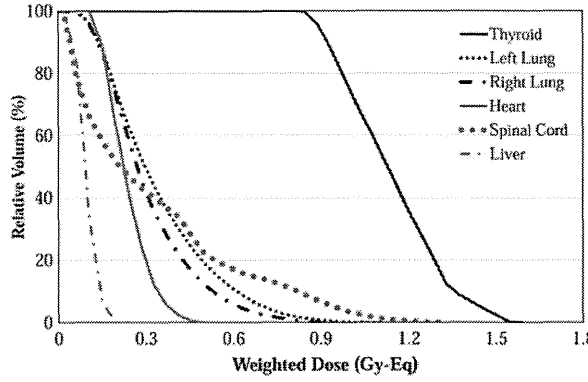

Figure 5. Expanded DVH of the undesirable dose for out-of-field organs during BNCT for a maxillary sinus tumour in the seated position.

dose evaluation using the Tsukuba-Plan, which allowed to create voxel models from a large numbers of medical images.

Wide-area dose evaluation during BNCT with the Tsukuba-Plan

The Monte Carlo calculation is one of the most accurate methods for particle transport and calculation[25]. However, maintaining statistical accuracy is a major impediment to using this method for dose evaluation, as a large number of particles must be transported to ensure statistical accuracy, which prolongs the calculation time.

Figure 6 shows the statistical uncertainties for the neutron fluence rate in a whole-body phantom, as calculated using the Monte Carlo code with various numbers of histories. For 1×10^9 histories, the statistical accuracy was inadequate in many areas, whereas the statistical accuracy was within 5 % for most areas when using 4×10^9 histories. However, the computational time with 4×10^9 histories took ~29.6 h on a parallel computing system with 70 cores. If the calculation mesh were set at a smaller size, the evaluation might require even more time for calculation. This reality might be accommodated by increasing the

Downloaded from http://rpd.oxfordjournals.org/ at National Cancer Centre (JMLA) on February 5, 2015

Table 3. $D_{average}$ **at various organs, including the CTV, during BNCT for a maxillary sinus tumour in the seated position.**

Organ	$D_{average}$ (Gy-Eq)
CTV	27.1
Thyroid	1.16
Right lung	0.33
Left lung	0.36
Heart	0.26
Spinal cord	0.34
Liver	0.12

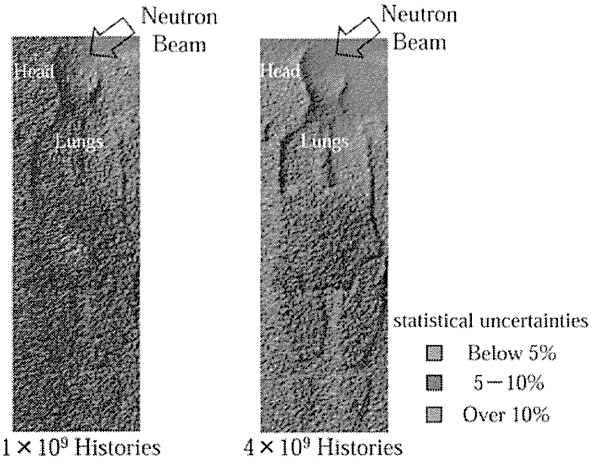

Figure 6. Comparison of the statistical uncertainties for the neutron fluence rate according to the number of histories. The figures show the coronal section of the whole-body phantom.

number of parallel computing cores, or by introducing the Monte Carlo calculation technique for variance reduction[25, 26] to increase the efficiency of the calculation. Alternatively, a larger voxel size and calculation mesh may be more efficient considering the statistical uncertainties.

The authors also calculated a voxel model of 16 pixels × 16 pixels × slice thickness for the whole-body phantom, using same number of parallel computing cores. This method's statistical accuracy was within 5 % for most areas when using only 2×10^9 histories, and the Monte Carlo calculation took ~13.4 h. However, using an excessively large voxel model may reduce the accuracy of the calculation. Therefore, it is not suitable for dose evaluation of the CTV and major organs at risk. In contrast, a combined voxel model, such as a small voxel model for the CTV combined with a large voxel model for the out-of-field organs, may make these calculations more useful. Therefore, this technique may shorten the total computation time, while maintaining the

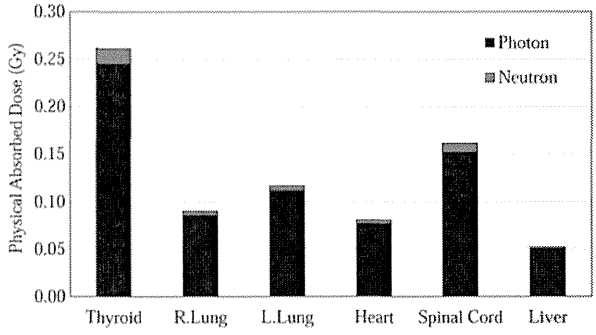

Figure 7. Averaged absorbed dose for the out-of-field organs during BNCT for a brain tumour in the supine position. Absorbed dose for neutron means the sum of the thermal neutron dose and the fast neutron dose.

calculation accuracy around the target area. This possibility will be rigorously examined in the future and is currently under development to allow the function that combines the various voxel sizes to be outputted.

Limitations

To evaluate the undesirable dose for the out-of-field organs using the Tsukuba-Plan, the photon dose, boron concentration and CBE of the various organs are all potential sources of uncertainties.

Photon dose

The photons generated by the interaction between neutrons and hydrogen atoms can be expressed using the following equation[22]:

$$^1\mathrm{H} + {}^1\mathrm{n} = {}^2\mathrm{H} + \gamma + 2.2\,\mathrm{MeV}$$

In addition, TLDs are frequently used to measure the photon dose in the BNCT irradiation field[27, 28]. The photon dose calculated using the Tsukuba-Plan was generally in agreement with the measured values for JRR-4, although a slight difference between the measured and calculated values was observed in the deep part of the phantom. This may be improved by fitting the beam source used in this study with the photons produced by JRR-4.

Boron concentration and CBE

In BNCT, the most effective dose component is the dose generated by boron. To calculate the boron dose, the CBE of the target organs and the amount of accumulated boron are critical. Unfortunately, the CBE values for the lung and liver were not derived using experimental data from JRR-4, and the JRR-4-specific CBE values for the other internal organs (such as the thyroid gland and heart) are also unknown. Thus,

Downloaded from http://iopscience.iop.org/ by National Cancer Center (JAERI) on 13 May 15

the authors assumed the CBE values of normal tissue for these organs. In addition, the boron concentrations for the internal organs outside of the irradiation field are not well known, and there is considerable uncertainty in this regard.

Evaluation of the undesirable radiation dose for out-of-field organs by using the absorbed dose

As mentioned, the authors attempted dose evaluation using the absorbed dose to decrease the uncertainties regarding the various assumptions mentioned earlier. For this evaluation, they set the boron concentration as 0, and the RBE values for the thermal neutron and the fast neutron as 1 (the same as a photon) for all the out-of-field organs. Absorbed dose for neutron is the sum of thermal neutron and fast neutron. Figure 7 shows the $D_{average}$ for photons and neutrons in the out-of-field organs, based on the absorbed dose during BNCT irradiation of a brain tumour in the supine position. The irradiation time was the same as for the evaluation with the biologically weighted dose. Figure 8 shows the $D_{average}$ of photons and neutrons in the out-of-field organs, based on the absorbed dose during BNCT irradiation of a maxillary sinus tumour in the seated position. The authors believe that this technique can estimate the scattering of photons and neutrons to the out-of-field organs, as the influence of boron on the out-of-field organ can be ignored. Based on the absorbed dose evaluation, it is evident that the influence of photons on the out-of-field organs is strong.

The role of Tsukuba-Plan as a comprehensive dose management system

In this study, the authors evaluated the undesirable dose to out-of-field organs during BNCT irradiation using the absorbed dose and the biological weighted dose. To evaluate the weighted dose, the authors assumed the CBE and boron concentration for the out-of-field organs, as BNCT is typically used to treat brain tumour, head and neck cancers, and therefore, the CBE and boron concentrations for the out-of-field organs are not well known. If BNCT were to be used more frequently to treat cancers in the body trunk, this might encourage further studies regarding the CBE and boron concentrations of the organs in the body trunk. This data would also enable the Tsukuba-Plan to more accurately calculate the specific organs' doses.

Interestingly, there have been reports of patients treated with a combination of BNCT and X-ray radiotherapy[17]. Presumably, the undesirable radiation dose for the healthy tissues is increased in these cases. Thus, it is important that RTP systems incorporate the capacity for dose evaluation for tumours and non-target areas.

In the past, when BNCT was combined with X-ray radiotherapy, it was necessary to manage the dose in each modality with separate RTP systems. However, the authors intend to equip the Tsukuba-Plan with the capacity to input the data in the DICOM-RT format, and this function will enable comprehensive dose management for combinations of BNCT and other radiotherapy.

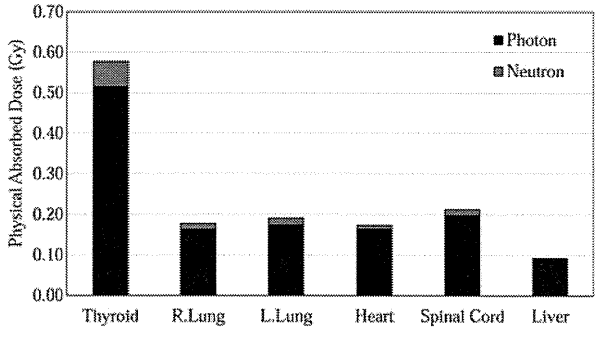

Figure 8. Averaged absorbed dose for the out-of-field organs during BNCT for a maxillary sinus tumour in the seated position. Absorbed dose for neutron means the sum of the thermal neutron dose and the fast neutron dose.

CONCLUSION

The authors used the Tsukuba-Plan, a recently developed BNCT treatment planning system, to estimate the undesirable radiation dose for a whole-body phantom during BNCT. The authors estimated the undesirable radiation dose as the absorbed dose and the biological weighted dose, using various assumptions for the CBE and boron concentrations in out-of-field organs. As the Tsukuba-Plan can be used to set the boron concentration and CBE for each organ, it is possible to calculate the absorbed dose or biologically weighted dose for each organ. Therefore, this system can calculate the undesirable whole-body radiation dose for BNCT during RTP, under patient-specific conditions, with a fine computational model generated by medical images.

REFERENCES

1. Locher, G. L. *Biological effects and therapeutic possibilities of neutrons.* Am. J. Roentgenol. Radium Ther. **36**, 1–13 (1936).
2. Tanaka, H., Sakurai, Y., Suzuki, M., Masunaga, S., Mitsumoto, T., Fujita, K., Kashino, G., Kinashi, Y., Liu, Y., Takada, M. *et al. Experimental verification of beam characteristics for cyclotron-based epithermal neutron source (C-BENS).* Appl. Radiat. Isot. **69**, 1642–1645 (2011).
3. Kumada, H., Matsumura, A., Sakurai, H., Sakae, T., Yoshioka, M., Kobayashi, H., Matsumoto, H., Kiyanagi, Y., Shibata, T. and Nakashima, H. *Project for the*

Downloaded from http://rpd.oxfordjournals.org/ at National Cancer Centre (JMLA) on February 5, 2015

development of the linac based NCT facility in University of Tsukuba. Appl. Radiat. Isot. **88**, 211–215 (2014).
4. Fleckenstein, J., Jahnke, L., Lohr, F., Wenz, F. and Hesser, J. *Development of a Geant4 based Monte Carlo Algorithm to evaluate the MONACO VMAT treatment accuracy.* Z. Med. Phys. **23**, 33–45 (2013).
5. Fotina, I., Winkler, P., Künzler, T., Reiterer, J., Simmat, I. and Georg, D. *Advanced kernel methods vs. Monte Carlo-based dose calculation for high energy photon beams.* Radiother. Oncol. **93**, 645–653 (2009).
6. Paganetti, H., Jiang, H., Lee, S. Y. and Kooy, H. M. *Accurate Monte Carlo simulations for nozzle design, commissioning and quality assurance for a proton radiation therapy facility.* Med. Phys. **31**, 2107–2118 (2004).
7. Hudson, F., Coulshed, D., D'Souza, E. and Baker, C. *Effect of radiation therapy on the latest generation of pacemakers and implantable cardioverter defibrillators: a systematic review.* J. Med. Imaging Radiat. Oncol. **54**, 53–61 (2010).
8. Gebhardt, R., Ludwig, M., Kirsner, S., Kisling, K. and Kosturakis, A. K. *Implanted intrathecal drug delivery systems and radiation treatment.* Pain Med. **14**, 398–402 (2013).
9. Fontenot, J. D., Lee, A. K. and Newhauser, W. D. *Risk of secondary malignant neoplasms from proton therapy and intensity-modulated x-ray therapy for early-stage prostate cancer.* Int. J. Radiat. Oncol. Biol. Phys. **74**, 616–622 (2009).
10. Athar, B. S. and Paganetti, H. *Comparison of second cancer risk due to out-of-field doses from 6-MV IMRT and proton therapy based on 6 pediatric patient treatment plans.* Radiother. Oncol. **98**, 87–92 (2011).
11. Sato, T., Niita, K., Matsuda, N., Hashimoto, S., Iwamoto, Y., Noda, S., Ogawa, T., Iwase, H., Nakashima, H., Fukahori, T. *et al. Particle and heavy ion transport code system, PHITS, version 2.52.* J. Nucl. Sci. Technol. **50**, 913–923 (2013).
12. Kumada, H., Yamamoto, K., Matsumura, A., Yamamoto, T., Nakagawa, Y., Nakai, K. and Kageji, T. *Verification of the computational dosimetry system in JAERI (JCDS) for boron neutron capture therapy.* Phys. Med. Biol. **49**, 3353–3365 (2004).
13. Yamamoto, T., Matsumura, A., Yamamoto, K., Kumada, H., Shibata, Y. and Nose, T. *In-phantom two-dimensional thermal neutron distribution for intraoperative boron neutron capture therapy of brain tumours.* Phys. Med. Biol. **47**, 2387–2396 (2002).
14. Horiguchi, H., Nakamura, T., Kumada, H., Yanagie, H., Suzuki, M. and Sagawa, H. *Investigation of irradiation conditions for recurrent breast cancer in JRR-4.* Appl. Radiat. Isot. **69**, 1882–1884 (2011).
15. Sakurai, Y., Tanaka, H., Suzuki, M., Masunaga, S., Kinashi, Y., Kondo, N., Ono, K. and Maruhashi, A. *Dose estimation for internal organs during boron neutron capture therapy for body-trunk tumors.* Appl. Radiat. Isot. **88**, 43–45 (2014).
16. Nakai, K., Kumada, H., Yamamoto, T., Tsurubuchi, T., Zaboronok, A. and Matsumura, A. *Feasibility of boron neutron capture therapy for malignant spinal tumors.* Appl Radiat Isot. **67**, S43–S46 (2009).
17. Yamamoto, T., Nakai, K., Nariai, T., Kumada, H., Okumura, T., Mizumoto, M., Tsuboi, K., Zaboronok, A., Ishikawa, E., Aiyama, H. *et al. The status of Tsukuba BNCT trial: BPA-based boron neutron capture therapy combined with X-ray irradiation.* Appl. Radiat. Isot. **69**, 1817–1818 (2011).
18. Kato, I., Ono, K., Sakurai, Y., Ohmae, M., Maruhashi, A., Imahori, Y., Kirihata, M., Nakazawa, M. and Yura, Y. *Effectiveness of BNCT for recurrent head and neck malignancies.* Appl. Radiat. Isot. **61**, 1069–1073 (2004).
19. Aihara, T., Morita, N., Kamitani, N., Kumada, H., Ono, K., Hiratsuka, J. and Harada, T. *Boron neutron capture therapy for advanced salivary gland carcinoma in head and neck.* Int. J. Clin. Oncol. **19**, 437–444 (2014).
20. Suzuki, M., Kato, I., Aihara, T., Hiratsuka, J., Yoshimura, K., Niimi, M., Kimura, Y., Ariyoshi, Y., Haginomori, S., Sakurai, Y. *et al. Boron neutron capture therapy outcomes for advanced or recurrent head and neck cancer.* J. Radiat. Res. **55**, 146–153 (2014).
21. Yamamoto, K., Kumada, H., Torii, Y., Kishi, T., Yamamoto, T. and Matsumura, A. *Simple estimation method of gamma-ray dose using low neutron-sensitive TLD (UD-170LS) for intra-operative boron neutron capture therapy (IOBNCT).* Res. Dev. Neutron Capture Ther. Editors: Sauerwein, W. *et al.*, Monduzzi Editore. **2002**, 499–503 (2002).
22. Hopewell, J. W., Morris, G. M., Schwint, A. and Coderre, J. A. *The radiobiological principles of boron neutron capture therapy: a critical review.* Appl. Radiat. Isot. **69**, 1756–1759 (2011).
23. Herrera, M. S., González, S. J., Minsky, D. M. and Kreiner, A. J. *Evaluation of performance of an accelerator-based BNCT facility for the treatment of different tumor targets.* Phys. Med. **29**, 436–446 (2013).
24. Tsukamoto, T., Tanaka, H., Yoshinaga, H., Mitsumoto, T., Maruhashi, A., Ono, K. and Sakurai, Y. *A phantom experiment for the evaluation of whole body exposure during BNCT using cyclotron-based epithermal neutron source (C-BENS).* Appl. Radiat. Isot. **69**, 1830–1833 (2011).
25. Haghighat, A. and Wagner, J. C. *Monte Carlo variance reduction with deterministic importance functions.* Prog. Nucl. Energ. **42**, 25–53 (2003).
26. Forster, R. A., Cox, L. J., Barrett, R. F., Booth, T. E., Briesmeister, J. F., Brown, F. B., Bull, J. S., Geisler, G. C., Goorley, J. T., Mosteller, R. D. *et al. MCNP*^{TM} *version 5.* Nucl. Instrum. Meth B. **213**, 82–86 (2004).
27. Aschen, C., Toivonen, M., Savolainen, S. and Stecher-Rasmussen, F. *Experimental correction for thermal neutron sensitivity of gamma-ray TL dosemeters irradiated at BNCT beams.* Radiat. Prot. Dosim. **82**, 65–69 (1999).
28. Sakurai, Y. and Kobayashi, T. *Characteristics of the KUR heavy water neutron irradiation facility as a neutron irradiation field with variable energy spectra.* Nucl. Instrum. Meth A. **453**, 569–596 (2000).

Journal of Radiation Research, 2014, 55, 658–664
doi: 10.1093/jrr/rru002 Advance Access Publication 21 March 2014

Increase in cell motility by carbon ion irradiation via the Rho signaling pathway and its inhibition by the ROCK inhibitor Y-27632 in lung adenocarcinoma A549 cells

Kazutoshi MURATA[1], Shin-ei NODA[1,*], Takahiro OIKE[1], Akihisa TAKAHASHI[2], Yukari YOSHIDA[3], Yoshiyuki SUZUKI[1], Tatsuya OHNO[3], Tomoo FUNAYAMA[4], Yasuhiko KOBAYASHI[4], Takeo TAKAHASHI[5] and Takashi NAKANO[1,3]

[1]Department of Radiation Oncology, Gunma University Graduate School of Medicine, 3-39-22, Showa-machi, Maebashi, Gunma 371-8511, Japan
[2]Advanced Scientific Research Leaders Development Unit, Gunma University, 3-39-22, Showa-machi, Maebashi, Gunma 371-8511, Japan
[3]Gunma University Heavy Ion Medical Center, 3-39-22, Showa-machi, Maebashi, Gunma 371-8511, Japan
[4]Microbeam Radiation Biology Group, Japan Atomic Energy Agency, Watanuki 1233, Takasaki, Gunma 370-1292, Japan
[5]Department of Radiation Oncology, Saitama Medical Center, Saitama Medical University, 1981, Kamoda, Kawagoe, Saitama 350-8550, Japan
*Corresponding author. Department of Radiation Oncology, Gunma University Graduate School of Medicine, 3-39-22, Showa-machi, Maebashi, Gunma 371-8511, Japan. Tel: +81-27-220-8383; Fax: +81-27-220-8397;
Email: snoda@gunma-u.ac.jp

(Received 19 August 2013; revised 8 December 2013; accepted 6 January 2014)

This study aimed to investigate the effect of carbon ion (C-ion) irradiation on cell motility through the ras homolog gene family member (Rho) signaling pathway in the human lung adenocarcinoma cell line A549. Cell motility was assessed by a wound-healing assay, and the formation of cell protrusions was evaluated by F-actin staining. Cell viability was examined by the WST-1 assay. The expression of myosin light chain 2 (MLC2) and the phosphorylation of MLC2 at Ser19 (P-MLC2-S19) were analyzed by Western blot. At 48 h after irradiation, the wound-healing assay demonstrated that migration was significantly greater in cells irradiated with C-ion (2 or 8 Gy) than in unirradiated cells. Similarly, F-actin staining showed that the formation of protrusions was significantly increased in cells irradiated with C-ion (2 or 8 Gy) compared with unirradiated cells. The observed increase in cell motility due to C-ion irradiation was similar to that observed due to X-ray irradiation. Western-blot analysis showed that C-ion irradiation (8 Gy) increased P-MLC2-S19 expression compared with in unirradiated controls, while total MLC2 expression was unchanged. Exposure to a non-toxic concentration of Y-27632, a specific inhibitor of Rho-associated coiled-coil-forming protein kinase (ROCK), reduced the expression of P-MLC2-S19 after C-ion irradiation (8 Gy), resulting in a significant reduction in migration. These data suggest that C-ion irradiation increases cell motility in A549 cells via the Rho signaling pathway and that ROCK inhibition reduces that effect.

Keywords: non-small cell lung carcinoma (NSCLC); cell motility; carbon ion (C-ion) irradiation; *ras* homolog gene family member (Rho); Rho-associated coiled-coil-forming protein kinase (ROCK)

INTRODUCTION

Non-small cell lung carcinoma (NSCLC) is one of the most lethal types of cancer, showing resistance to conventional radiation therapy (RT) [1]. Carbon ion (C-ion) RT is considered to be a promising treatment strategy for early-stage NSCLC because (i) C-ion RT is superior to conventional X-ray RT in dose distributions, with higher concentrations in tumors and superior normal tissue sparing that enables dose escalations, and (ii) a C-ion beam has a higher relative biological effectiveness (RBE) than that of X-rays. In fact, a previous study demonstrated favorable local control achieved by C-ion RT in patients with early-stage NSCLC [2]; however, another previous study documented cases with marginal

© The Author 2014. Published by Oxford University Press on behalf of The Japan Radiation Research Society and Japanese Society for Radiation Oncology. This is an Open Access article distributed under the terms of the Creative Commons Attribution License (http://creativecommons.org/licenses/by/4.0/), which permits unrestricted reuse, distribution, and reproduction in any medium, provided the original work is properly cited.

recurrence after C-ion RT, which is an issue of great importance [3]. Marginal recurrence in C-ion RT may be due, in part, to insufficient dose delivery with a steep dose fall-off and susceptibility to set-up error and organ motion at the margin of tumors. Another possible cause for marginal recurrence is increased cancer-cell motility after irradiation. Several *in vitro* studies demonstrated that X-ray irradiation increased cell motility in cancer cells of various origins, including lung [4–6]. These reports indicate the possibility that cancer cells receiving X-ray irradiation may move outside of the radiation fields in clinical settings.

The increase in cancer-cell motility due to X-ray irradiation is achieved through the *ras* homolog gene family member (Rho) signaling pathway [5, 7]. In the Rho signaling pathway, Rho-associated coiled-coil-forming protein kinase (ROCK) is considered to act as an effector downstream of Rho [8]. ROCK directly and indirectly phosphorylates myosin light chain 2 (MLC2) at Ser19 (P-MLC2-S19), thereby increasing the contractility of actomyosin, which forms stress fibers and cell protrusions, resulting in cell migration. However, the effect of C-ion irradiation on motility in NSCLC cells and the underlying mechanisms have not been fully elucidated. Therefore, the present study investigated motility in A549 lung adenocarcinoma cells exposed to C-ion irradiation *in vitro*. The involvement of the Rho signaling pathway in radiation-induced motility was assessed using Y-27632, a specific inhibitor of ROCK [9].

MATERIALS AND METHODS

Cells and materials

A549 cells were purchased from the Cell Resources Center for Biomedical Research in Tohoku University (Sendai, Japan). The cells were cultured in RPMI-1640 (Invitrogen, CA, USA) supplemented with 10% fetal bovine serum (ICN Biomedicals, OH, USA) at 37°C with 5% CO_2. Y-27632, a specific inhibitor of ROCK, was purchased from Merck (Darmstadt, Germany).

Carbon ion and X-ray irradiation

C-ion irradiation was performed at the Takasaki Ion Accelerators for Advanced Radiation Application in the Japan Atomic Energy Agency (Gunma, Japan) or Gunma Heavy Ion Medical Center (Gunma, Japan). C-ion beams with a linear energy transfer of 108 keV/μm were used. The RBE of the C-ion irradiation in A549 cells at a 10% surviving fraction was calculated as 3.9 by a clonogenic survival assay (Supplementary Fig. 1).

WST-1 assay

To assess the viability of A549 cells, a WST-1 assay (Roche, Mannheim, Germany) was performed according to the manufacturer's instructions. A549 cells were seeded on 96-well plates (1.0×10^4 cells/well) and incubated at 37°C for 12 h.

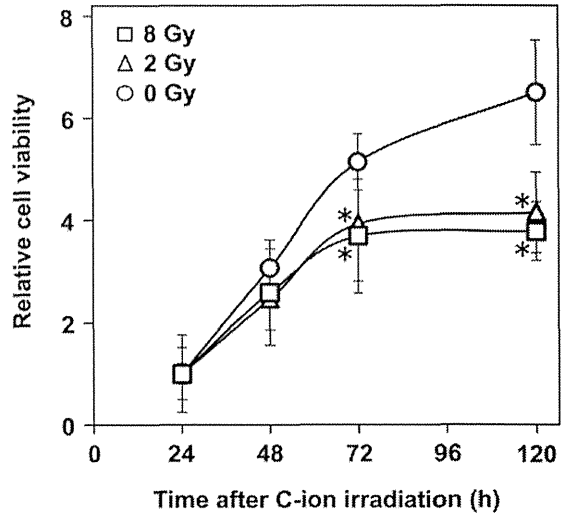

Fig. 1. The effect of carbon (C-ion) irradiation on the viability of A549 cells assessed by WST-1 assay. An asterisk indicates significant difference compared with the unirradiated control.

The cells received C-ion irradiation (0, 2 or 8 Gy) or continuous exposure to Y-27632 (0.01, 0.1, 1, 10 or 50 μM). After incubating for 24, 48, 72 or 120 h, 20 μl of WST-1 reagent was applied to each well. After incubating for an additional 3 h at 37°C, absorption of 450 nm light was measured using a Multiskan FC (Thermo, Helsinki, Finland).

Wound-healing assay

The motility of A549 cells was assessed by wound-healing assay, as previously described [7]. Briefly, A549 cells were cultured on 35-mm culture dishes to confluence. The monolayers were wounded by scratching with sterile pipette tips, rinsed once with culture medium, and then exposed to fresh culture medium. The cells were then subjected to C-ion irradiation (2 or 8 Gy) and incubated at 37°C for 2, 6, 12, 24 or 48 h. Phase-contrast images of the wounds were obtained at a × 20 magnification using a Real Surface View Microscope VE-7800 (Keyence, Osaka, Japan). For each wound, the distance between the nuclei of the cells located on the two edges of a wound was measured at 30 points in the vertical direction to the axis of the wound; the average value was defined as the width of the wound. The distance the cells migrated was calculated by subtracting the width of the wound measured at a given timepoint from that obtained 2 h after irradiation. To assess the effect of Y-27632, the cells were continuously exposed to 30 μM Y-27632 from 18 h before wounding to image acquisition.

F-actin staining

A549 cells seeded on coverslips were cultured for 18 h at 37°C to achieve 50% confluence, and then subjected (or not) to X-ray (8 Gy) or C-ion irradiation (2 or 8 Gy). After culturing

for a further 24 h, the cells were fixed with 3.7% paraformaldehyde for 10 min at room temperature, and permeabilized with 0.2% Triton X-100 for 5 min. The specimens were incubated with the actin stain 488 phalloidin (Cytoskeleton Inc., CO, USA) for 30 min at 37°C according to the manufacturer's instruction, and counter-stained with DAPI for 5 min. To evaluate the formation of cell protrusions, the cells were imaged using a Real Surface View Microscope VE-7800 (Keyence) at a ×20 magnification. Five independent cell counts of at least 100 cells each were performed for each set of experimental conditions. The cells were counted by two researchers (K.M. and T.O.), blind to the experimental conditions, and evaluated for the formation of cell protrusions.

Western-blot analysis

A549 cells were cultured in the presence or absence of Y-27632 (30 μM) for 18 h and subjected (or not) to C-ion irradiation (2 or 8 Gy). After incubating for a further 0.5, 2 or 24 h at 37°C, the cells were harvested and lysed with cell lysis buffer (Millipore, MA, USA) containing phosphatase inhibitor cocktails 1 and 2 (Sigma-Aldrich, MO, USA) and protease inhibitor cocktail 3 (Calbiochem, Darmstadt, Germany). The protein lysates (50 μg) were subjected to electrophoresis on 15% mini-PROTEAN TGX precast gels (Bio-Rad, CA, USA) and transferred to nitrocellulose membranes (Bio-Rad). The membranes were incubated at room temperature for 1 h with PBST supplemented with 5% skimmed milk and exposed to primary and secondary antibodies. Primary antibodies specific for the following proteins were used: MLC2 (Cell Signaling Technology, MA, USA), P-MLC2-S19 (Cell Signaling Technology) and β-actin (Chemicon International, CA, USA). A polyclonal goat anti-mouse immunoglobulin (DAKO, CA, USA) was used as a secondary antibody. The Western blots were visualized using ECL chemiluminescent reagents (Bio-Rad) and ChemiStage CC16 mini (Wealtec, NV, USA).

Statistics

Significant differences were analyzed by an unpaired two-tailed Student's t-test. $P < 0.05$ was considered significant. Results are expressed as the mean ± standard deviation (SD) of values obtained from at least three independent experiments. The error bars in the figures represent SDs.

RESULTS

Carbon ion irradiation increased cell motility in A549 cells

First we examined the effect of C-ion irradiation on the motility of A549 cells. Prior to the assessment of cell motility, the viability of C-ion-irradiated cells was assessed because differences in viability among cells receiving different doses of C-ion irradiation might affect the motility assessment. The WST-1 assay showed that the viability of the unirradiated cells increased from 24 to 120 h (Fig. 1). Meanwhile, C-ion irradiation (2 and 8 Gy) significantly reduced the cell viability 72 and 120 h after the irradiation (2 Gy, $P = 0.0026$ and 0.000 70; 8 Gy, $P = 0.013$ and 0.0027, respectively); however, 48 h after receiving C-ion irradiation, there were no significant differences in viability between the irradiated and unirradiated cells (0 Gy vs 2 Gy, $P = 0.22$; 0 Gy vs 8 Gy, $P = 0.49$). As a result of these data, the assessment of cell motility was performed within 48 h after irradiation, a period when C-ion irradiation did not significantly affect cell viability.

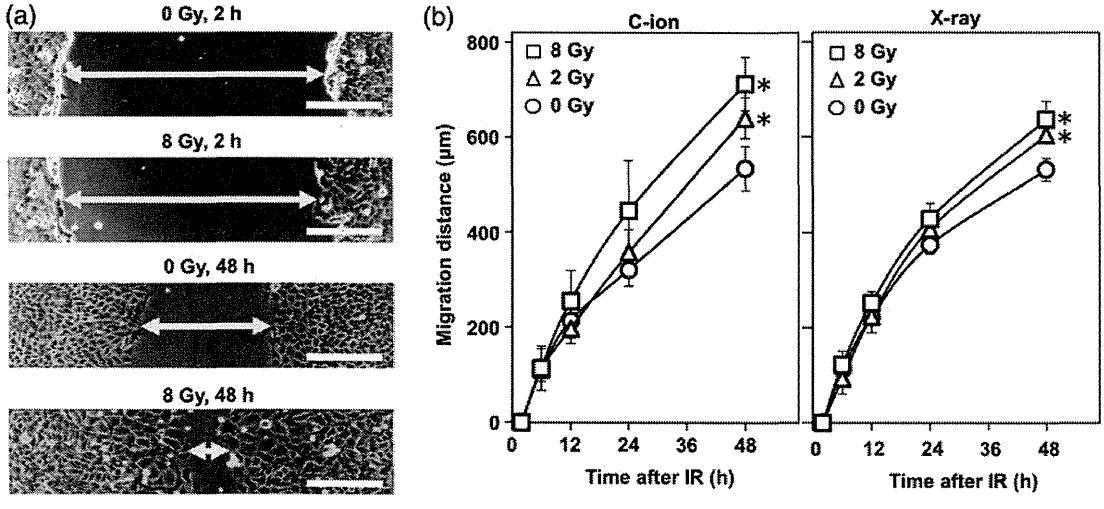

Fig. 2. The effect of carbon ion (C-ion) and X-ray irradiation on cell motility in A549 cells assessed by a wound-healing assay. **(a)** Representative micrographs of the wounds observed 2 and 48 h after receiving C-ion irradiation. The arrow indicates the width of a wound. Scale bar, 200 μm. **(b)** Distances the cells migrated. Left panel, cells receiving C-ion irradiation; right panel, cells receiving X-ray irradiation. An asterisk indicates significant difference compared with the corresponding unirradiated control.

The effect of C-ion irradiation on cell motility was assessed by wound-healing assay (Fig. 2a and b). At 48 h after receiving C-ion irradiation for 0, 2 or 8 Gy, the distance the cells migrated was 534 ± 47, 640 ± 43 and 712 ± 56 μm, respectively. The migration distance was significantly greater in the cells irradiated with 2 and 8 Gy than in the unirradiated cells (P = 0.045 and 0.013, respectively). It appeared that there was a dose-dependence in the increase in cell motility.

Meanwhile, the wound-healing assay showed that X-ray irradiation also increased the motility of A549 cells (Fig. 2b). At 48 h after X-ray irradiation (2 and 8 Gy), when cell viability was not significantly affected (data not shown), the cells receiving 0, 2 and 8 Gy migrated 531.52 ± 23.67, 604.12 ± 16.55 and 637.58 ± 38.35 μm, respectively. The migration distance was significantly greater in the cells receiving X-ray irradiation (2 and 8 Gy) than in the unirradiated cells (P = 0.012 and 0.015, respectively).

To further investigate the effect of C-ion and X-ray irradiation on cell motility, we evaluated the formation of cell protrusions, another marker of motility [10], by F-actin staining. Interestingly, irradiation with both C-ion (2 and 8 Gy) and X-rays (8 Gy) significantly increased the formation of cell protrusions 24 h after irradiation compared with unirradiated controls (C-ion, P = 0.0026 and 0.000 039 for 2 and 8 Gy, respectively; X-rays, P = 0.000 28 for 8 Gy) (Fig. 3). Taken together, these data suggest that C-ion irradiation increases cell motility in A549 cells in a similar manner to X-rays.

ROCK inhibition by Y-27632 suppressed the increase in motility in A549 cells after carbon ion irradiation

The Rho signaling pathway is involved in the increase in cell motility after X-ray irradiation in A549 cells [7]. Therefore, the involvement of the Rho signaling pathway in the increase

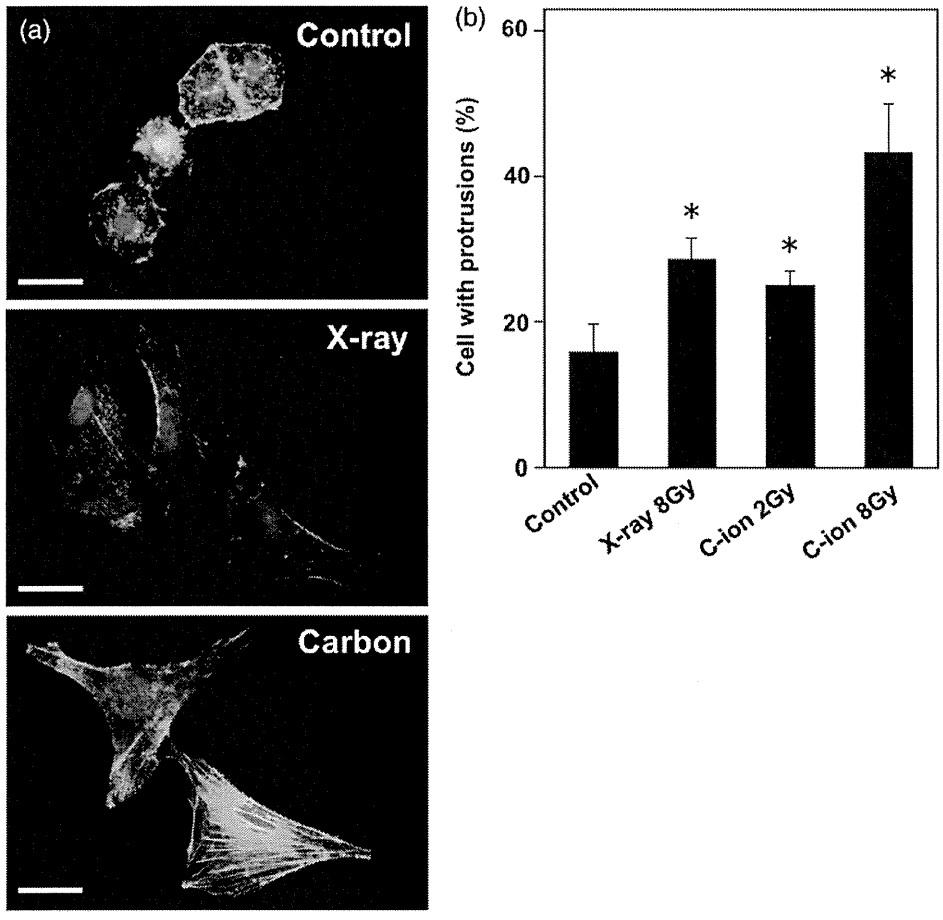

Fig. 3. The effect of carbon ion (C-ion) and X-ray irradiation on the formation of cell protrusions in A549 cells assessed by F-actin staining. **(a)** Representative micrograph of non-treated control cells (upper panel), cells irradiated with X-rays for 8 Gy (middle panel), and those irradiated with C-ion for 8 Gy (lower panel) taken 24 h after irradiation at a ×40 magnification. F-actin and nuclei are shown in green (Alexa Fluor 488 phaloidin) and blue (DAPI), respectively. Scale bar, 30 μm. **(b)** Numbers of cells forming protrusions are shown. An asterisk indicates significant difference compared with the unirradiated control.

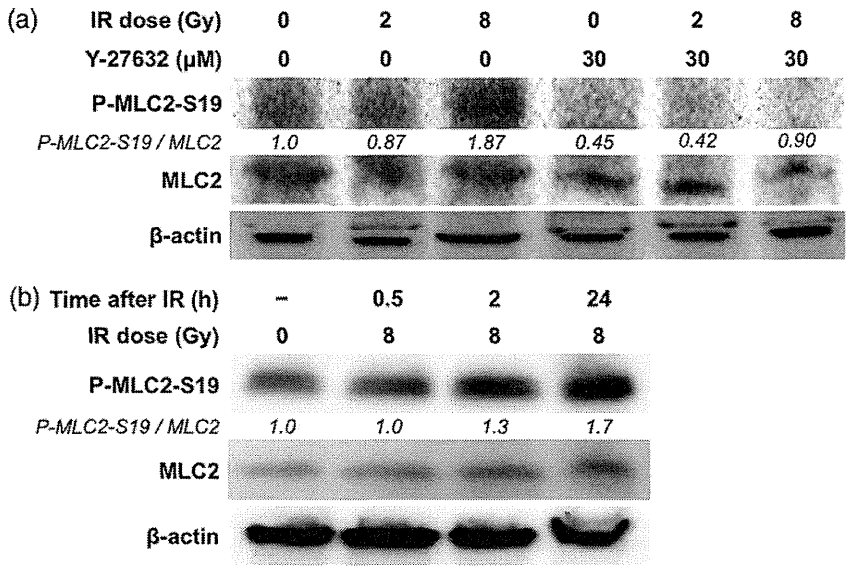

Fig. 4. The effects of carbon ion (C-ion) irradiation and/or Y-27632 on the phosphorylation of myosin light chain 2 (MLC2) in A549 cells assessed by Western blot. The ratio of the expression level of phosphorylated MLC2 at Ser19 (P-MLC2-S19) to that of MLC2 is shown. The ratios were normalized with respect to the non-treated control. β-actin is shown as a loading control. IR = irradiation. **(a)** Expression of MLC2 and P-MLC2-S19 in cells exposed to C-ion IR (2 or 8 Gy) and/or Y-27632 (30 μM) 24 h after irradiation. **(b)** Expression of MLC2 and P-MLC2-S19 in cells irradiated with C-ion (8 Gy) 0.5, 2 or 24 h after irradiation.

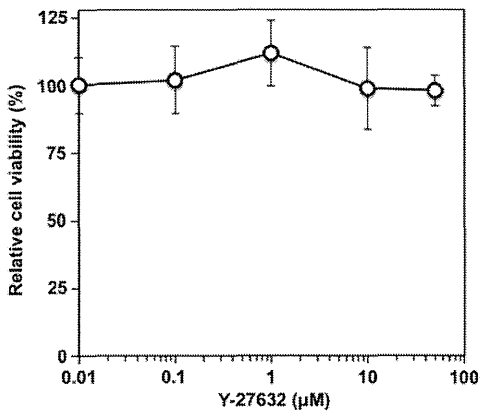

Fig. 5. The effect of Y-27632 on the viability of A549 cells. The cells were exposed to Y-27632 for 48 h and subjected to a WST-1 assay. The viability of cells were normalized with respect to that of cells exposed to 0.01 μM Y-27632.

in cell motility after C-ion irradiation in A549 cells was investigated by Western blot. At 24 h after C-ion irradiation, increased P-MLC2-S19 expression was observed in cells irradiated with 8 Gy compared with unirradiated controls (Fig. 4a). Interestingly, the phosphorylation level of MLC2 increased in a time-dependent manner (Fig. 4b). These results indicate that activation of the Rho signaling pathway may contribute to the increase in cell motility in A549 cells receiving C-ion irradiation. Therefore, we investigated whether the inhibition of ROCK suppressed the increase in cell motility by C-ion irradiation using Y-27632, which is a specific inhibitor of ROCK. A WST-1 assay showed that there was no significant difference in the viability of the cells exposed to Y-27632 at concentrations ranging from 0.01 to 50 μM for 48 h (Fig. 5). From these results, 30 μM, a concentration at which Y-27632 does not affect cell viability, was used in subsequent analyses. Western-blot analysis showed that the expression of P-MLC2-S19 was reduced in all the samples exposed to Y-27632 (Fig. 4a). Of note, Y-27632 reduced the expression of P-MLC2-S19 in cells receiving C-ion (8 Gy) to a level similar to that observed in non-treated controls, indicating that Y-27632 suppressed signal transduction through the Rho/ROCK/MLC2 pathway activated after C-ion irradiation. Wound-healing assays revealed that Y-27632 significantly reduced the migration distance of the irradiated cells (P = 0.049 and 0.039 for 2 and 8 Gy, respectively) (Fig. 6). Taken together, these data indicate that inhibition of ROCK reduces the increase in cell motility after C-ion irradiation in A549 cells.

DISCUSSION

In the present study, wound-healing assays and F-actin staining showed that C-ion irradiation increased cell motility in A549 cells. It seems that the increase in cancer-cell motility after irradiation is not a characteristic of C-ion beams, but rather a phenomenon similar to what is observed after X-ray

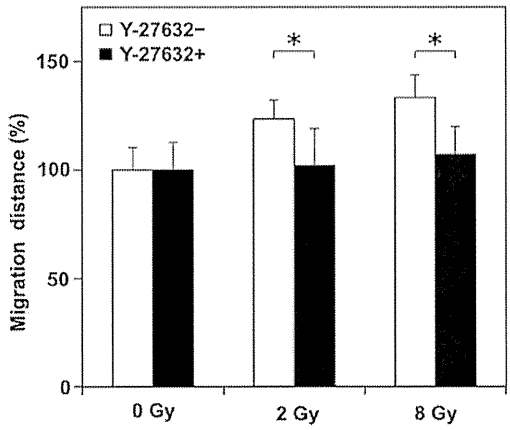

Fig. 6. The effect of Y-27632 on motility in A549 cells after C-ion irradiation assessed by a wound-healing assay. The cells were exposed to Y-27632 (30 μM) for 18 h and subjected to a wound-healing assay as in Fig. 2. The cells were kept exposed to Y-27632 until the time of assessment. For each of the samples treated with or without Y-27632, the migration distances were compared with those of unirradiated controls. The asterisk indicates significant difference.

irradiation. We also found that the Rho/ROCK/MLC2 signaling pathway, which can be targeted by the ROCK inhibitor Y-27632, was involved in the increase in cell motility in A549 cells after C-ion irradiation, suggesting that ROCK inhibition may reduce the migration of the irradiated cancer cells when used in combination with C-ion RT.

Several *in vitro* studies investigated the effect of C-ion irradiation on the migration of cancer cells [11, 12]. In these, C-ion irradiation suppressed the migration of cancer cells (U87 glioma cells and HCT116 colon carcinoma cells by Goetze *et al.*; EBC-1 lung squamous cell carcinoma cells and A549 cells by Akino *et al.*). These results are in contrast to ours, possibly due to the difference in the assay system employed. Our study used a wound-healing assay and evaluated the migration of cells in a horizontal direction on culture dishes. Meanwhile, Goetze *et al.* [11] and Akino *et al.* [12] used a Boyden chamber assay in which the numbers of cells that pass through a filter with narrow pores in a vertical direction are counted. Moreover, the studies by Goetze *et al.* and Akino *et al.* employed filters precoated with collagens. Cancer cells utilize proteolytic enzymes such as matrix metalloproteinases to degrade the extracellular matrix, including collagens, and generate a path for moving through it [13]. Therefore, in the studies by Goetze *et al.* and Akino *et al.*, the effect of C-ion irradiation on the activity of proteolytic enzymes may be reflected in the results. Further investigation is required to elucidate the effect of C-ion irradiation on cell motility, proteolytic enzyme activity and other mechanisms involved in cancer invasion and metastasis.

The results of the present study indicate that cell motility in A549 cells is increased by C-ion irradiation with 2 and 8 Gy, calculated as 7.8 and 31.2 GyRBE, respectively. The irradiation dose per fraction used in C-ion RT for early-stage NSCLC at Gunma University Heavy Ion Medical Center falls within this range (i.e. 13.2–15.0 GyRBE/fraction; a total of 52.8–60.0 GyRBE is delivered in four fractions in one week). Therefore, although it is crude to directly extrapolate *in vitro* data into the clinical setting, the results of the wound-healing assay suggest a potential clinical benefit. In fact, the migration distance of the irradiated cells scored in the wound-healing assay corresponded to 0.53–0.71 mm per day. These data may be informative in defining clinical target volumes in actual treatment planning. To further explore this issue, the effect of the fractionated C-ion irradiation on cancer-cell motility should be examined.

The Rho signaling pathway involving in the cell motility has many downstream effectors. Among them, in the present study, we selected the phosphorylation of MLC2 at Ser19 as an indicator of the activation of Rho signaling because it is well known that the Ser19 of MLC2 is specifically phosphorylated via ROCK [14], and that the resulting P-MLC2-S19 plays a pivotal role in cell motility through its interaction with actin–myosin [15]. There is a clinically available (intravenously administered) agent with ROCK inhibitory activity named fasudil (Daiichi Chemical and Pharmacological Company, Ibaragi, Japan), which is approved in Japan for the prevention of cerebral vasospasm in patients with subarachnoid hemorrhage [16]. In this regard, if the involvement of the Rho/ROCK/MLC2 cascade in the increased cancer-cell motility after C-ion irradiation is proven, the finding can be directly applied in the clinic with fasudil treatment combined with C-ion RT for the prevention of cancer-cell migration after C-ion RT. However, fasudil is known to interact with multiple molecules such as free intracellular calcium ions and protein kinases A, G and C (16). Thus, in the present study, in order to clearly evaluate the effect of ROCK inhibition on cell motility after C-ion irradiation, the inhibitor Y-27632, which is specific for ROCK [17], was used instead of fasudil, even though Y-27632 is not suitable for human use. As a result, ROCK inhibition by Y-27632 resulted in the reduced motility in A549 cells irradiated with C-ion of 2 and 8 Gy by 20% and 25%, respectively (Fig. 6). These data indicate the potential of clinical ROCK inhibition for the suppression of migration of cancer cells during and after C-ion RT. Taken together, fasudil combined with C-ion RT is an attractive method for improving local disease control that warrants investigation in the clinic.

The present study has several limitations. In a wound-healing assay, only the motility of cells at the edge of scratched wounds can be evaluated. In contrast, in F-actin staining, cells seeded on coverslips at 50% confluence showed increased cell protrusions, indicating that C-ion irradiation increased cell motility not only in cells living on the edge of tumors, but also in those living at the center of a cluster of cancer cells. Nevertheless, these results are not

enough to completely understand the spatio-temporal effect of C-ion irradiation on cancer-cell motility. The present study also investigated the effect of C-ion irradiation on cancer-cell motility within 48 h after irradiation, when C-ion irradiation did not significantly affect cell viability, in order to focus on motility; however, in the clinical setting the situation can be more complicated because the repopulation of the irradiated cancer cells may affect their motility. To clarify these issues, analyses using 3D tumor models such as *in vitro* spheroids or *in vivo* mouse xenograft tumor models should be performed in the future. Furthermore, the mechanism underlying the continuous phosphorylation of MLC2-S19 after C-ion irradiation is largely unknown and warrants further investigation.

CONCLUSION

In conclusion, the present study showed that C-ion irradiation increased cell motility in A549 cells via the Rho/ROCK/MLC2 signaling pathway, and that inhibition of ROCK reduced the increase in cell motility in irradiated cells. Further investigation will elucidate the effect of C-ion irradiation on migration, invasion and metastasis, and the underlying mechanism, which will help to develop efficient treatment strategies in C-ion RT.

SUPPLEMENTARY DATA

Supplementary data is available at the *Journal of Radiation Research* online.

FUNDING

This work was supported by Grant-in-Aid for Young Scientists (B) from the Japan Society for the Promotion of Science Grant Number 25861071.

REFERENCES

1. Rosenzweig KE, Sura S, Jackson A *et al.* Involved-field radiation therapy for inoperable non–small-cell lung cancer. *J Clin Oncol* 2007;**25**:5557–61.
2. Miyamoto T, Baba M, Yamamoto N *et al.* Curative treatment of stage I non-small-cell lung cancer with carbon ion beams using a hypofractionated regimen. *Int J Radiat Oncol Biol Phys* 2007;**67**:750–8.
3. Koto M, Miyamoto T, Yamamoto N *et al.* Local control and recurrence of stage I non-small cell lung cancer after carbon ion radiotherapy. *Radiother Oncol* 2004;**71**:147–56.
4. Cordes N, Meineke V. Cell adhesion-mediated radioresistance (CAM-RR). Extracellular matrix-dependent improvement of cell survival in human tumor and normal cells *in vitro*. *Strahlenther Onkol* 2003;**179**:337–44.
5. Fujita M, Otsuka Y, Yamada S *et al.* X-ray irradiation and Rho-kinase inhibitor additively induce invasiveness of the cells of the pancreatic cancer line, MIAPaCa-2, which exhibits mesenchymal and amoeboid motility. *Cancer Sci* 2011;**102**:792–8.
6. Zhai GG, Malhotra R, Delaney M *et al.* Radiation enhances the invasive potential of primary glioblastoma cells via activation of the Rho signaling pathway. *J Neurooncol* 2006;**76**:227–37.
7. Zhu F, Zhang Z, Wu G *et al.* Rho kinase inhibitor fasudil suppresses migration and invasion though down-regulating the expression of VEGF in lung cancer cell line A549. *Med Oncol* 2011;**28**:565–71.
8. Nakagawa O, Fujisawa K, Ishizaki T *et al.* ROCK-I and ROCK-II, two isoforms of Rho-associated coiled-coil forming protein serine/threonine kinase in mice. *FEBS Lett* 1996;**392**:189–93.
9. Uehata M, Ishizaki T, Satoh H *et al.* Calcium sensitization of smooth muscle mediated by a Rho-associated protein kinase in hypertension. *Nature* 1997;**389**:990–4.
10. Machacek M, Hodgson L, Welch C *et al.* Coordination of Rho GTPase activities during cell protrusion. *Nature* 2009;**461**:99–103.
11. Goetze K, Scholz M, Taucher-Scholz G *et al.* The impact of conventional and heavy ion irradiation on tumor cell migration *in vitro*. *Int J Radiat Biol* 2007;**83**:889–96.
12. Akino Y, Teshima T, Kihara A *et al.* Carbon-ion beam irradiation effectively suppresses migration and invasion of human non-small-cell lung cancer cells. *Int J Radiat Oncol Biol Phys* 2009;**75**:475–81.
13. Wie LH, Lai KP, Chen CA *et al.* Arsenic trioxide prevents radiation-enhanced tumor invasiveness and inhibits matrix metalloproteinase-9 through downregulation of nuclear factor κB. *Oncogene* 2005;**25**:390–8.
14. Ridley AJ. Rho family proteins: coordinating cell responses. *Trends Cell Biol* 2001;**11**:471–7.
15. Amano M, Ito M, Kimura K *et al.* Phosphorylation and activation of myosin by Rho-associated kinase (Rho-kinase). *J Biol Chem* 1996;**34**:20246–9.
16. Shibuya M, Suzuki Y, Sugita K *et al.* Effect of AT877 on cerebral vasospasm after aneurysmal subarachnoid hemorrhage. Results of a prospective placebo-controlled double-blind trial. *J Neurosurg* 1992;**76**:571–7.
17. Honjo M, Tanihara H, Inatani M *et al.* Effects of rho-associated protein kinase inhibitor Y-27632 on intraocular pressure and outflow facility. *Invest Ophthalmol Vis Sci* 2001;**42**:137–44.

Journal of Radiation Research, 2014, 55, 713–719
doi: 10.1093/jrr/rru015 Advance Access Publication 4 April 2014

Cranial irradiation induces bone marrow-derived microglia in adult mouse brain tissue

Noriyuki OKONOGI[1], Kazuhiro NAKAMURA[2], Yoshiyuki SUZUKI[1], Nana SUTO[2], Kazutomo SUZUE[3], Takuya KAMINUMA[1], Takashi NAKANO[1] and Hirokazu HIRAI[2,*]

[1]Department of Radiation Oncology, Gunma University Graduate School of Medicine, 3-39-22 Showa-machi, Maebashi, Gunma 371-8511, Japan
[2]Department of Neurophysiology, Gunma University Graduate School of Medicine, 3-39-22 Showa-machi, Maebashi, Gunma 371-8511, Japan
[3]Department of Parasitology, Gunma University Graduate School of Medicine, 3-39-22 Showa-machi, Maebashi, Gunma 371-8511, Japan
*Corresponding author. Department of Neurophysiology, Gunma University Graduate School of Medicine 3-39-22 Showa-machi, Maebashi, Gunma 371-8511, Japan. Tel: +81-27-220-7930; Fax: +81-27-220-7936; Email: hirai@gunma-u.ac.jp

(Received 25 November 2013; revised 16 February 2014; accepted 21 February 2014)

Postnatal hematopoietic progenitor cells do not contribute to microglial homeostasis in adult mice under normal conditions. However, previous studies using whole-body irradiation and bone marrow (BM) transplantation models have shown that adult BM cells migrate into the brain tissue and differentiate into microglia (BM-derived microglia; BMDM). Here, we investigated whether cranial irradiation alone was sufficient to induce the generation of BMDM in the adult mouse brain. Transgenic mice that express green fluorescent protein (GFP) under the control of a murine stem cell virus (MSCV) promoter (MSCV-GFP mice) were used. MSCV-GFP mice express GFP in BM cells but not in the resident microglia in the brain. Therefore, these mice allowed us to detect BM-derived cells in the brain without BM reconstitution. MSCV–GFP mice, aged 8–12 weeks, received 13.0 Gy irradiation only to the cranium, and BM-derived cells in the brain were quantified at 3 and 8 weeks after irradiation. No BM-derived cells were detected in control non-irradiated MSCV-GFP mouse brains, but numerous GFP-labeled BM-derived cells were present in the brain stem, basal ganglia and cerebral cortex of the irradiated MSCV-GFP mice. These BM-derived cells were positive for Iba1, a marker for microglia, indicating that GFP-positive BM-derived cells were microglial in nature. The population of BMDM was significantly greater at 8 weeks post-irradiation than at 3 weeks post-irradiation in all brain regions examined. Our results clearly show that cranial irradiation alone is sufficient to induce the generation of BMDM in the adult mouse.

Keywords: microglia; bone marrow-derived microglia; cranial irradiation; transgenic mice

INTRODUCTION

Microglia are immune effector cells of the central nervous system (CNS) and play an important role in processes such as phagocytosis [1] and antigen-presentation [2], and in defense against the neurodegeneration of neural tissue [3]. In the prenatal state, hematopoietic progenitor cells differentiate into microglia. However, under normal conditions in the postnatal state, hematopoietic progenitor cells do not contribute to microglial homeostasis in the adult mouse [4]. However, recent studies have shown that adult bone marrow (BM) cells may have the potential to migrate to the brain tissue and differentiate into microglia under non-normal conditions [5, 6]. Microglia that have migrated from the BM to the adult brain tissue have been termed BM-derived microglia (BMDM).

The combination of BM transplantation with whole-body irradiation is one specific condition that induces BMDM formation. Priller *et al.* have reported that sublethal whole-body irradiation given as a pretreatment to BM transplantation induced the migration of BM cells to the adult mouse brain [5]. They concluded that BM transplantation, rather than

© The Author 2014. Published by Oxford University Press on behalf of The Japan Radiation Research Society and Japanese Society for Radiation Oncology. This is an Open Access article distributed under the terms of the Creative Commons Attribution License (http://creativecommons.org/licenses/by/4.0/), which permits unrestricted reuse, distribution, and reproduction in any medium, provided the original work is properly cited.

irradiation, primarily contributes to the induction of BM cells seen in the brain tissue. In a different study, Burrell *et al.* showed that irradiation alone would induce the migration of BM cells into the brain [6]. In Burrell's study, sublethal irradiation to the whole-body except for the cranial region was given prior to BM transplantation. The mice then received cranial irradiation after BM reconstitution. This resulted in BM cell migration to the irradiated brain region. The authors further showed that the majority of migrated BM cells had differentiated into microglia. They concluded that irradiation alone induced the migration of BM cells into the brain. However, the experiment by Burrell *et al.* included both BM transplantation and sublethal whole-body irradiation. Therefore, it remains unclear whether irradiation, specifically, cranial irradiation, alone is sufficient to induce BMDM generation or if co-treatment with BM transplantation is required.

In the present study, transgenic mice expressing green fluorescent protein (GFP) in the BM cells, but not in brain-resident microglia, were used. We examined whether cranial irradiation is sufficient to induce BMDM in the adult mouse brain. We further determined the brain regions preferentially targeted during migration and the temporal change in BMDM number following cranial irradiation.

MATERIALS AND METHODS

Animals

All experiments were conducted in accordance with the guidelines of the Animal Care and Experimentation Committee of the Gunma University. The experimental design is shown in Fig. 1A. We used only male transgenic mice at the age of 8–12 weeks with a C57BL/6 background, which expressed GFP under the control of murine stem cell virus (MSCV) promoter (MSCV-GFP mice) [7]. Mice were subjected to cranial irradiation. MSCV–GFP mice express GFP in BM cells and cerebellar Purkinje cells but not in resident microglia [8], which enabled us to detect endogenous BM cells that migrate into the brain tissue without BM reconstitution.

Cranial irradiation

Cranial irradiation was performed using a TITAN 225-S X-ray machine (Shimadzu Co., Tokyo, Japan) that generated 200 kV X-rays at a dose rate of 1.3 Gy/min. Mice were anesthetized with an intraperitoneal injection of pentobarbital (40 mg/kg), and were placed in a prone position. A lead plate (6 mm thick) containing a rectangular window was positioned over the mouse to shield the majority of the body (Fig. 1B) but allow exposure to just the head of the mouse through the window. This resulted in cranial region-specific irradiation. A total of 13 Gy of cranial irradiation was applied to the dorsal side of each mouse. MSCV–GFP mice aged 8–12 weeks received cranial irradiation ($n = 8$). Animals that underwent the same anesthesia protocol but did not receive irradiation served as a control group ($n = 4$) (Fig. 1).

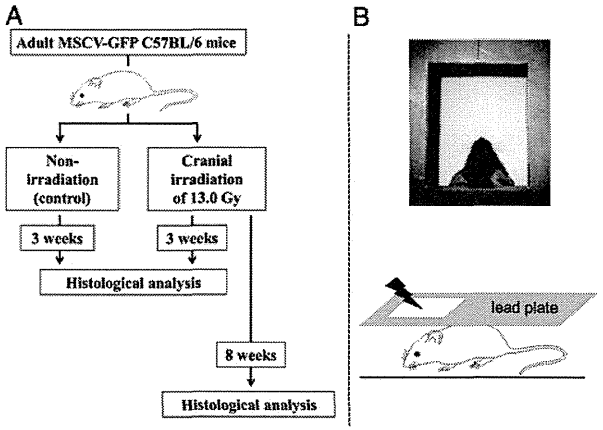

Fig. 1. Experimental design. (**A**) Schematic depicting the experimental protocol. Eight MSCV-GFP mice received 13 Gy cranial irradiation under anesthesia. Four MSCV-GFP mice that received anesthesia but were not subjected to irradiation were used as controls. Four irradiated and four non-irradiated mice were sacrificed for histological analysis 3 weeks post-treatment. The remaining four irradiated mice were sacrificed and histologically examined at 8 weeks post-irradiation. (**B**) For head-specific irradiation, a mouse was placed in the prone position, and the body except for the cranial region was shielded with lead plates.

Immunofluorescent staining

Irradiated MSCV–GFP mice were sacrificed at 3 weeks ($n = 4$) or 8 weeks ($n = 4$) after treatment for histological analysis. Control MSCV-GFP mice that received only anesthesia were similarly examined at 3 weeks ($n = 4$) after the treatment.

Transcardial perfusion with 4% paraformaldehyde in phosphate-buffered saline (PBS) was performed prior to brain dissection. Dissected brain tissue was fixed in the same fixative solution for an additional 24 h. On the next day, the brains were washed in PBS and cut into 50-μm sagittal sections using a vibratome. The sections were double immunostained with rat monoclonal anti-GFP (1:1000; 04404-84; Nacalai Tesque, Kyoto, Japan) and rabbit polyclonal anti-Iba1 (1:1000; 019-19741; Wako, Osaka, Japan) antibodies, as described previously [9]. In brief, sections were incubated in the presence of 1 μg/ml anti-Iba1 and 1 μg/ml anti-GFP antibodies overnight. After three PBS washes, sections were incubated with the fluorescent secondary antibodies, Alexa Fluor 488 donkey anti-rat IgG (1:1000; Life Technologies, Gaithersburg, MD, USA) and Alexa Fluor 568 donkey anti-rabbit IgG (1:1000; Life Technologies) in PBS for 1 h at room temperature. The stained sections were mounted on glass slides after three PBS washes. We have confirmed that the immunoreactivity was specific by conducting negative

control experiments that included secondary antibodies, but not primary antibodies.

Quantification of resident microglia and bone marrow-derived microglia

All sections were observed by the blind test method. All fluorescent images were obtained using a fluorescence microscope (BZ-9000; Keyence, Osaka, Japan) equipped with a ×20 objective lens. We counted the number of cells in five randomly selected regions/slice. In each focused brain region, five to six slices from four animals/group were used for the analysis. Sections were excited at 488 nm and 543 nm. All fluorescent images were analyzed with the BZ-II analysis program (Keyence). Both GFP- and Iba1-positive cells were automatically counted (Figs 2–4) and were further confirmed by visual inspection. In brief, the contrast of all obtained images was adjusted to the same condition (shadows: 60, Highlight: 150, γ-value: 1.0) in BZ-II analysis program (Keyence). Then, Keyence's 'cell separation method' was used to count individual cells. Cells <10 μm^2 were excluded from counting. Microglia were immunolabeled for Iba1. Iba1-positive cells that were co-immunostained for GFP were derived from the BM and were therefore considered to be BMDM. The numbers of Iba1-positive and GFP-negative cells and Iba1- and GFP-double positive cells in 1 mm^2 were counted.

Statistical analysis

Significant differences were evaluated using ANOVA with a *post hoc* test and an unpaired two-tailed Student's *t*-test. Data were analyzed using group means with error bars reported as standard deviations (SDs). Differences were considered significant when the *P*-values were <0.05. All statistical analyses were performed using SPSS 16.0 for Mac (SPSS, Chicago, IL, USA).

RESULTS

Migration of BMDM into the brain tissue

Fig. 2A – C shows representative fluorescence images of the brain stem double immunostained for Iba1 and GFP from non-irradiated MSCV-GFP mice (Fig. 2A) and from irradiated MSCV-GFP mice at 3 (Fig. 2B) and 8 (Fig. 2C) weeks after cranial irradiation. Iba1-positive microglia were widely distributed in all groups. Quantitative data analysis showed that the number of resident microglia, which were

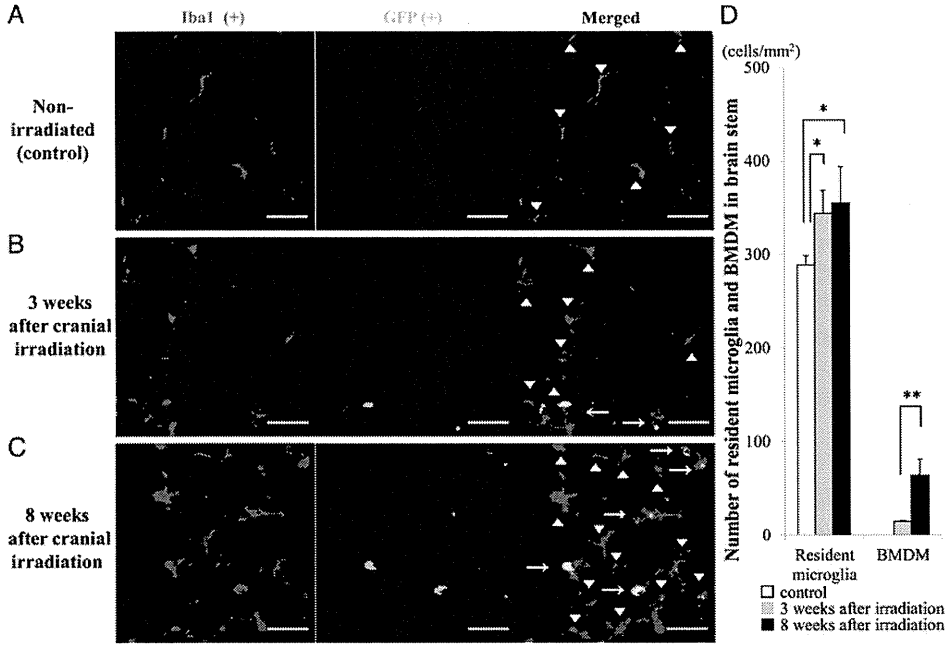

Fig. 2. Induction of BMDM in the brain tissue following the cranial irradiation. (A–C) Representative images of the brain stem double immunolabeled for GFP and Iba1 from non-irradiated control mice (**A**) and irradiated mice at 3 (**B**) and 8 (**C**) weeks post-irradiation. Iba1-positive and GFP-negative resident microglial cells were observed in all groups (arrowheads), whereas Iba1- and GFP- double positive cells were present only in the irradiated groups (arrows). Scale bars, 40 μm. (**D**) Summarized graph showing the number of resident microglia (left columns) and BMDM (right columns) in 1 mm^2 area of the brain stem. White bar: control group, gray bars: 3 weeks post-irradiation, black bars: 8 weeks post-irradiation. *$P < 0.05$, **$P < 0.01$.

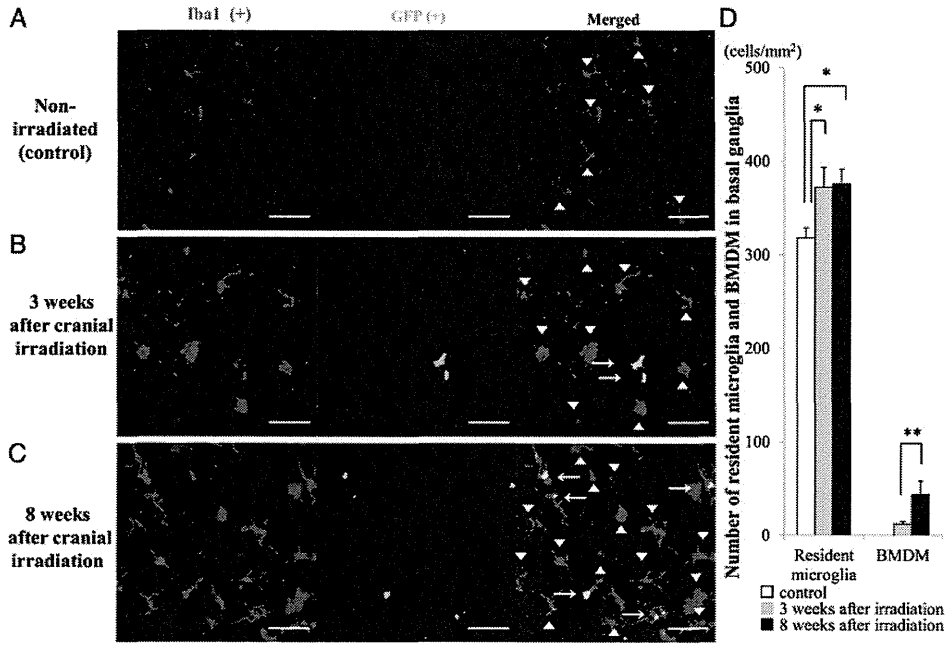

Fig. 3. Migration of BMDM in the basal ganglia after the cranial irradiation. (A–C) Representative images of the basal ganglia double immunolabeled for GFP and Iba1 from non-irradiated control mice (**A**) and irradiated mice at 3 (**B**) and 8 (**C**) weeks post-irradiation. Similar to the brain stem, Iba1-positive and GFP-negative resident microglial cells were observed in all groups (arrowheads), and Iba1- and GFP-double-positive cells were present only in the irradiated groups (arrows). Scale bars, 40 μm. (**D**) Summarized graph showing the number of resident microglia (left columns) and BMDM (right columns) in 1 mm^2 area of the basal ganglia. White bar: control group, gray bars: 3 weeks post-irradiation, black bars: 8 weeks post-irradiation. $*P < 0.05$, $**P < 0.01$.

defined as Iba1-positive and GFP-negative cells (arrowheads in Fig. 2A–C), was significantly higher at 3 ($P < 0.05$) and 8 ($P < 0.05$) weeks post-irradiation compared with non-irradiated controls (Fig. 2D). Notably, Iba1- and GFP-double positive cells (arrows in Fig. 2B and C), which were considered to be BMDM (hereafter referred to as BMDM), were observed only in the irradiated groups. Moreover, the density of BMDM was significantly higher at 8 weeks post-irradiation than at 3 weeks post-irradiation ($P < 0.01$, Fig. 2D).

Similar patterns were found in the basal ganglia (Fig. 3A – C) and cerebral cortex (Fig. 4A – C). The number of resident microglia in these regions was significantly higher in irradiated mice at both 3 ($P < 0.05$, each) and 8 weeks post-irradiation ($P < 0.05$, each), compared with the control, non-irradiated mice (Figs 3D and 4D). Similar to what was observed in the brain stem, Iba1- and GFP-double positive BMDM were also observed in these regions in the irradiated groups but not in the non-irradiated group.

Comparison of the number of resident microglia and BMDM in different brain regions

Figure 5A and B show a time-course for the number of resident microglia and BMDM observed in the brain stem, basal ganglia, and cerebral cortex after cranial irradiation. Resident microglia density was almost comparable in the brain stem (290 ± 10 cells/mm^2) and the basal ganglia (318 ± 11 cells/mm^2) of control, non-irradiated mice, whereas it was significantly less in the cerebral cortex (184 ± 28 cells/mm^2). As described above, cranial irradiation significantly increased resident microglia density in all three regions to 339–373 cells/mm^2 at 3 weeks post-irradiation. No statistically significant differences in number were present between the groups (Fig. 5A). The resident microglia density in these three regions at 8 weeks after irradiation ranged from 341–376 cells/mm^2, showing no further increase in the resident microglia population (Fig. 5A).

In contrast, the number of BMDM increased in a manner dependent on the time following irradiation. The number of BMDM at 3 weeks post-irradiation was highest in the brain stem (15 ± 1 cells/mm^2), followed by the basal ganglia (12 ± 3 cells/mm^2) and cerebral cortex (7 ± 3 cells/mm^2). The number of BMDM in the cerebral cortex was significantly less than that in the brain stem (Fig. 5B). The difference between BMDM numbers in the brain regions expanded at 8 weeks post-irradiation. The number of BMDM at 8 weeks post-irradiation was 64 ± 17 cells/mm^2 in the brain stem, 44 ± 15 cells/mm^2 in the basal ganglia, and 19 ± 1 cells/mm^2 in the cerebral cortex. Thus, the number of BMDM in each region increased 2.7–4.3 times during the

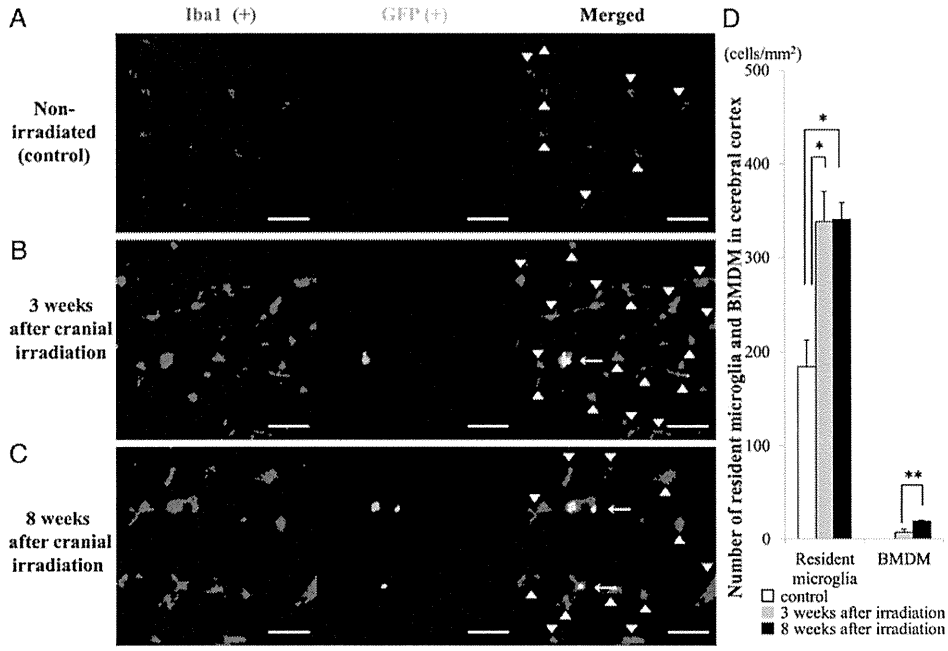

Fig. 4. Migration of BMDM in the cerebral cortex after the cranial irradiation. (A–C) Representative images of the cerebral cortex double immunolabeled for GFP and Iba1 from non-irradiated control mice (**A**) and irradiated mice at 3 (**B**) and 8 (**C**) weeks post-irradiation. Similar to other regions, Iba1-positive and GFP-negative resident microglial cells were observed in all groups (arrowheads), and Iba1- and GFP-double-positive cells were present only in the irradiated groups (arrows). Scale bars, 40 μm. (**D**) Summarized graph showing the number of resident microglia (left columns) and BMDM (right columns) in 1 mm^2 area of the cerebral cortex. White bar: control group, gray bars: 3 weeks post-irradiation, black bars: 8 weeks post-irradiation. $*P < 0.05$, $**P < 0.01$.

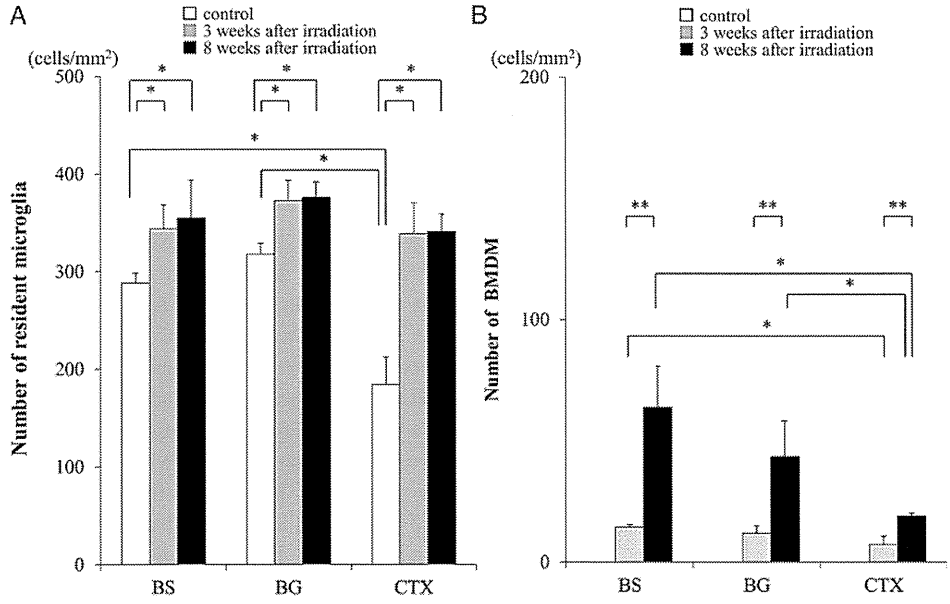

Fig. 5. Regional differences in the number of resident microglia and BMDM. (A, B) Comparison of the number of resident microglia (**A**) and BMDM (**B**) in the brain stem (BS), basal ganglia (BG), and cerebral cortex (CTX) between control, non-irradiated mice (white columns) and irradiated mice at 3 (gray columns) or 8 (black columns) weeks post-irradiation. All values are presented as the mean ± SD, $*P < 0.05$, $**P < 0.01$.